

Doping evolution of nodal electron dynamics in trilayer cuprate superconductor $Bi_2Sr_2Ca_2Cu_3O_{10+\delta}$ revealed by laser-based angle-resolved photoemission spectroscopy

Hao Chen(陈浩), Jumin Shi(史聚民), Xiangyu Luo(罗翔宇), Yinghao Li(李颖昊), Yiwen Chen(陈逸雯), Chaohui Yin(殷超辉), Yingjie Shu(束英杰), Jiuxiang Zhang(张九相), Taimin Miao(苗泰民), Bo Liang(梁波), Wenpei Zhu(朱文培), Neng Cai(蔡能), Xiaolin Ren(任晓琳), Chengtian Lin(林成天), Shenjin Zhang(张申金), Zhimin Wang(王志敏), Fengfeng Zhang(张丰丰), Feng Yang(杨峰), Qinjun Peng(彭钦军), Zuyan Xu(许祖彦), Guodong Liu(刘国东), Hanqing Mao(毛寒青), Xintong Li(李昕彤), Lin Zhao(赵林), X. J. Zhou(周兴江)
Citation: Chin. Phys. B, 2025, 34 (**7**): 077404. DOI: 10.1088/1674-1056/addcc6
http://cpb.iphy.ac.cn; http://iopscience.iop.org/cpb

What follows is a list of articles you may be interested in

Experimental observation of Fermi-level flat band in novel kagome metal $CeNi_5$

Xue-Zhi Chen(陈学智), Le Wang(王乐), Shuai Zhang(张帅), Ren-Jie Zhang(张任杰), Yi-Wei Cheng(程以伟), Yu-Dong Hu(胡裕栋), Cheng-Nuo Meng(孟承诺), Zheng-Tai Liu(刘正太), Bai-Qing Lv(吕佰晴), and Yao-Bo Huang(黄耀波)
Chin. Phys. B, 2024, 33 (**8**): 087402. DOI: 10.1088/1674-1056/ad4019

Manipulation of band gap in 1*T*-$TiSe_2$ via rubidium deposition

Yi Ou(欧仪), Lei Chen(陈磊), Zi-Ming Xin(信子鸣), Yu-Jing Ren(任宇靖), Peng-Hao Yuan(袁鹏浩), Zheng-Guo Wang(王政国), Yu Zhu(朱玉), Jing-Zhi Chen(陈景芝), and Yan Zhang(张焱)
Chin. Phys. B, 2024, 33 (**8**): 087401. DOI: 10.1088/1674-1056/ad48f9

Surface doping manipulation of the insulating ground states in $Ta_2Pd_3Te_5$ and $Ta_2Ni_3Te_5$

Bei Jiang(江北), Jingyu Yao(姚静宇), Dayu Yan(闫大禹), Zhaopeng Guo(郭照芃), Gexing Qu(屈歌星), Xiutong Deng(邓修同), Yaobo Huang(黄耀波), Hong Ding(丁洪), Youguo Shi(石友国), Zhijun Wang(王志俊), and Tian Qian(钱天)
Chin. Phys. B, 2024, 33 (**6**): 067402. DOI: 10.1088/1674-1056/ad362e

Electronic structure and effective mass of pristine and Cl-doped $CsPbBr_3$

Zhiyuan Wei(魏志远), Yu-Hao Wei(魏愉昊), Shendong Xu(徐申东), Shuting Peng(彭舒婷), Makoto Hashimoto, Donghui Lu(路东辉), Xu Pan(潘旭), Min-Quan Kuang(匡泯泉), Zhengguo Xiao(肖正国), and Junfeng He(何俊峰)
Chin. Phys. B, 2024, 33 (**5**): 057403. DOI: 10.1088/1674-1056/ad3c31

Extremely fast vortex dynamics in $Bi_2Sr_2Ca_2Cu_3O_{10+\delta}$ crystalline nanostrip

A B Yu(于奥博), C T Lin(林成天), X F Zhang(张孝富), and L X You(尤立星)
Chin. Phys. B, 2023, 32 (**6**): 067402. DOI: 10.1088/1674-1056/acb425

RAPID COMMUNICATION

Doping evolution of nodal electron dynamics in trilayer cuprate superconductor $Bi_2Sr_2Ca_2Cu_3O_{10+\delta}$ revealed by laser-based angle-resolved photoemission spectroscopy

Hao Chen(陈浩)[1,2,†], Jumin Shi(史聚民)[1,2,†], Xiangyu Luo(罗翔宇)[1], Yinghao Li(李颖昊)[1,2], Yiwen Chen(陈逸雯)[1,2], Chaohui Yin(殷超辉)[1], Yingjie Shu(束英杰)[1,2], Jiuxiang Zhang(张九相)[1,2], Taimin Miao(苗泰民)[1,2], Bo Liang(梁波)[1,2], Wenpei Zhu(朱文培)[1,2], Neng Cai(蔡能)[1,2], Xiaolin Ren(任晓琳)[1,2], Chengtian Lin(林成天)[3], Shenjin Zhang(张申金)[4], Zhimin Wang(王志敏)[4], Fengfeng Zhang(张丰丰)[4], Feng Yang(杨峰)[4], Qinjun Peng(彭钦军)[4], Zuyan Xu(许祖彦)[4], Guodong Liu(刘国东)[1,2,5], Hanqing Mao(毛寒青)[1,2,5], Xintong Li(李昕彤)[1,2,5], Lin Zhao(赵林)[1,2,5,‡], and X. J. Zhou(周兴江)[1,2,5,§]

[1] *Beijing National Laboratory for Condensed Matter Physics, Institute of Physics, Chinese Academy of Sciences, Beijing* 100190, *China*
[2] *University of Chinese Academy of Sciences, Beijing* 100049, *China*
[3] *Max Planck Institute for Solid State Research, Heisenbergstrasse* 1, *D-70569 Stuttgart, Germany*
[4] *Technical Institute of Physics and Chemistry, Chinese Academy of Sciences, Beijing* 100190, *China*
[5] *Songshan Lake Materials Laboratory, Dongguan* 523808, *China*

(Received 22 May 2025; revised manuscript received 22 May 2025; accepted manuscript online 23 May 2025)

The doping evolution of the nodal electron dynamics in the trilayer cuprate superconductor $Bi_2Sr_2Ca_2Cu_3O_{10+\delta}$ (Bi2223) is investigated using high-resolution laser-based angle-resolved photoemission spectroscopy (ARPES). Bi2223 single crystals with different doping levels are prepared by controlled annealing, which cover the underdoped, optimally-doped and overdoped regions. The electronic phase diagram of Bi2223 is established which describes the T_c dependence on the sample doping level. The doping dependence of the nodal Fermi momentum for the outer (OP) and inner (IP) CuO_2 planes is determined. Charge distribution imbalance between the OP and IP CuO_2 planes is quantified, showing enhanced disparity with increasing doping. Nodal band dispersions demonstrate a prominent kink at $\sim$ 94 meV in the IP band, attributed to the unique Cu coordination in the IP plane, while a weaker $\sim$ 60 meV kink is observed in the OP band. The nodal Fermi velocity of both OP and IP bands is nearly constant at $\sim$ 1.62 eV·Å independent of doping. These results provide important information to understand the origin of high T_c and superconductivity mechanism in high temperature cuprate superconductors.

Keywords: Bi2223, angle-resolved photoemission spectroscopy, nodal electron dynamics, doping evolution
PACS: 74.25.Dw, 74.25.Jb, 74.72.–h
DOI: 10.1088/1674-1056/addcc6 **CSTR:** 32038.14.CPB.addcc6

The trilayer cuprates (Fig. 1(a)) are unique among all the discovered cuprate superconductors.[1] First, it has been found that the superconducting transition temperature (T_c) depends sensitively on the number of CuO_2 planes (n) per structural unit and the trilayer cuprates give the highest T_c among the same family.[1–5] Second, the trilayer cuprates exhibit an unusual electronic phase diagram distinct from that established for the single-layer and bilayer cuprates.[6] In the general phase diagram, T_c goes up with increasing doping in the underdoped region, reaches a maximum at the optimal doping, and then decreases to zero in the overdoped region. But in the trilayer cuprate $Bi_2Sr_2Ca_2Cu_3O_{10+\delta}$ (Bi2223), while T_c increases with increasing doping in the underdoped region, it stays nearly constant in the overdoped region.[7,8] The electronic structure studies of the trilayer cuprates are important to understand the origin of the high T_c and the superconductivity mechanism. However, due to the sample limitation, the angle-resolved photoemission (ARPES) measurements on Bi2223 are rather scarce and mostly focused on the optimally-doped samples.[9–17]

In this paper, we prepared a series of Bi2223 single crystal samples with various doping levels by annealing the samples under different conditions. We carried out high-resolution laser-based ARPES measurements on the nodal electronic structures of these samples. The doping dependence of the charge distribution among the three CuO_2 planes is determined in Bi2223. The evolution of the nodal electron dynamics with doping is revealed.

High-resolution ARPES measurements were carried out using our lab-based ARPES system equipped with a 6.994 eV

[†]These authors contributed equally to this work.
[‡]Corresponding author. E-mail: LZhao@iphy.ac.cn
[§]Corresponding author. E-mail: XJZhou@iphy.ac.cn
© 2025 Chinese Physical Society and IOP Publishing Ltd. All rights, including for text and data mining, AI training, and similar technologies, are reserved.

vacuum ultraviolet (VUV) laser and an angle-resolved time-of-flight (ARToF) electron energy analyzer, as well as another laser-based ARPES setup utilizing a 6.994 eV VUV laser and a DA30L hemispherical electron energy analyzer (Scienta-Omicron).[18,19] The ARToF ARPES system enables simultaneous acquisition of photoelectrons across two-dimensional momentum space (k_x, k_y). For both ARPES systems, the energy resolution was set at ~ 1 meV, and the angular resolution was approximately 0.3°. All Bi2223 samples were cleaved *in situ* at low temperature and measured in ultrahigh vacuum with a base pressure better than 5×10^{-11} Torr. The Fermi level was referenced by measuring a clean polycrystalline gold which was electrically connected to the sample.

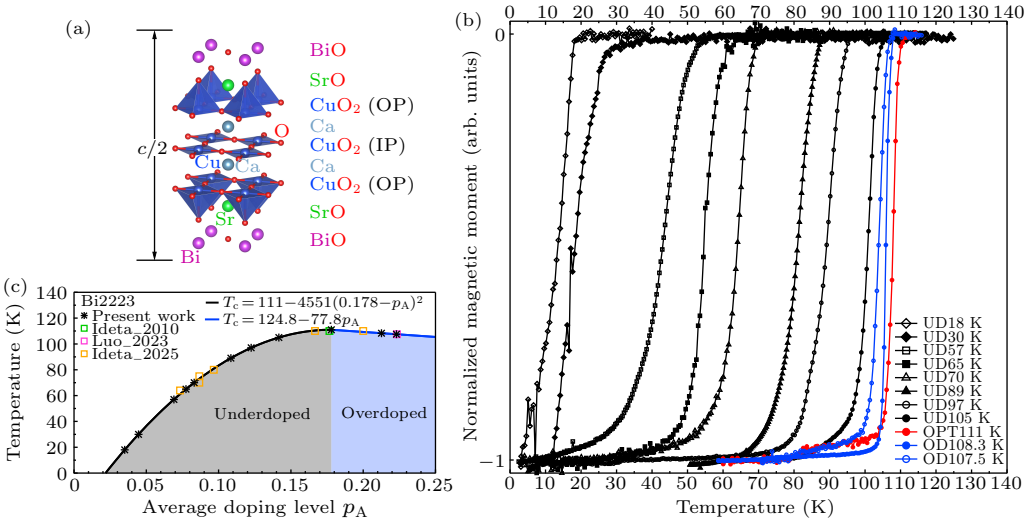


Fig. 1. Preparation of Bi2223 single crystals with different doping levels and the related phase diagram. (a) Schematic crystal structure of Bi2223. Here only half of the unit cell is drawn and the complete unit cell consists of two such structural units displaced with each other by ($a/2$, $b/2$). Each structural unit contains three adjacent CuO_2 planes with one inner plane (IP) and two outer planes (OPs). (b) AC magnetic measurements of Bi2223 single crystals with different doping levels and different T_cs. The optimally-doped Bi2223 single crystals have a T_c at 111 K. The optimally-doped samples were annealed in vacuum to obtain underdoped samples with T_cs at 105 K, 97 K, 89 K, 70 K, 65 K, 57 K, 30 K and 18 K. The optimally-doped samples were also annealed under high oxygen pressure of $\sim$ 170 atmospheres to obtain overdoped samples with T_cs at 108.3 K and 107.5 K. (c) Phase diagram of Bi2223. The underdoped region is obtained by fitting the data of T_cs and doping levels from previous studies with a parabolic form while the overdoped region is obtained by fitting the previous data of T_cs and doping levels with a linear form.[11,16,17] Here the doping level p_A refers to the average value of doping levels on all the three CuO_2 planes (p_C). The doping levels of our samples with different T_cs are determined based on this phase diagram.

Bi2223 single crystals were grown by the traveling-solvent floating-zone method.[20,21] The samples were characterized by AC magnetic measurements (Fig. 1(b)) and T_c is defined by the onset of the Meissner effect. The optimally-doped (OPT) samples were obtained by annealing the as-grown Bi2223 single crystals in air and they have a T_c of 111 K. Then the optimally-doped Bi2223 samples were annealed under two different conditions to adjust their doping levels. To get the underdoped (UD) samples, the optimally-doped samples were annealed in vacuum (1×10^{-3} mbar) at different temperatures for different durations.[7,8,20–23] As listed in Table 1 and shown in Fig. 1(b), the underdoped, heavily underdoped and even non-superconducting Bi2223 samples can be obtained. To reach the overdoped (OD) region, the optimally-doped samples were annealed under high oxygen pressure ($\sim$ 170 atmospheres) at various temperatures for different durations,[7,8,16,22] as shown in Fig. 1(b). For the overdoped samples, we find that T_c is nearly a constant; it only slightly decreases with the increasing doping. The most overdoped Bi2223 sample has a T_c at 107.5 K. For convenience, we name our Bi2223 samples by their doping state (underdoped, optimally-doped and overdoped) and T_c. For example, UD57 K represents the Bi2223 sample which is underdoped and has a T_c at 57 K.

Table 1. Preparation of underdoped Bi2223 samples with different T_cs by annealing the optimally-doped sample in vaccum at different temperatures for different durations.

Annealing temperature	Annealing duration, T_c						
500 °C	1 h	4 h	4.5 h	5.5 h	8 h	10 h	33 h
	108 K	88 K	88 K	69 K	60 K	30 K	NSC
450 °C	15 h	24 h	48 h	41 h	72 h		
	42 K	32 K	19 K	NSC	NSC		
420 °C	15 h	18.5 h	72 h	72 h	96 h		
	47 K	22 K	33 K	35 K	34 K		
400 °C	15 h	24 h	81 h				
	80 K	59 K	40 K				

Although the T_c dependence on the doping level is qualitatively observed in Bi2223,[7,8] the phase diagram is still lacking to quantitatively describe the relation between T_c and the doping level. To establish such a phase diagram, Bi2223 samples covering the underdoped, optimally-doped and overdoped regions are required. Their T_cs need to be precisely measured and the corresponding doping levels need to be determined. Based on the previous ARPES measurements on Bi2223,[11,16,17] we established the electronic phase diagram of Bi2223 as shown in Fig. 1(c). On the underdoped side, we fitted the data from the underdoped samples[17] (orange squares) and the optimally-doped sample[11] (green

squares) by assuming a parabolic form and obtained the relation $T_c = 111 - 4551(0.178 - p_A)^2$, as shown by the black line in Fig. 1(c). On the overdoped side, we fitted the data from the optimally-doped sample[11] (green squares) and the overdoped sample[17] (pink squares) by assuming a linear form and obtained the relation $T_c = 124.8 - 77.8p_A$, as shown by the blue line in Fig. 1(c). By combining the underdoped and overdoped regions, we established the quantitative relation between T_c and the doping level in Bi2223. When T_c of the Bi2223 samples is measured (Fig. 1(b)), their corresponding doping levels can be determined as shown by asterisks in Fig. 1(c) for our samples.

Figure 2(a) shows a typical Fermi surface mapping in the UD105 K Bi2223 sample measured at 15 K by using our ARToF-ARPES system. Since our laser-ARPES measurements can cover only a small portion of the Brillouin zone, the position of the Fermi surface mapping, particularly along the nodal direction, is determined by referring to the previous ARPES measurements on Bi2223 samples.[11,16,17] Two main Fermi surface sheets are clearly observed, labelled as OP and IP in Fig. 2(a). The OP and IP Fermi surface sheets originate mainly from the outer CuO_2 planes and the inner CuO_2 plane, respectively. The separation of these two Fermi surface sheets reflects the difference of charge carrier distribution among the OP and IP CuO_2 planes. Since the outer CuO_2 planes are adjacent to the charge reservoir layers, the doping level of the outer planes is higher than that of the inner plane. This charge distribution imbalance has been observed in the NMR and STEM measurements of the multilayer cuprates.[24,25]

Figure 2(b) displays band structures of Bi2223 with different doping levels measured at 15 K along the nodal momentum cut that is indicated as the black line in Fig. 2(a). Here the UD57 K, UD70 K, UD89 K, UD105 K and OD108.3 K Bi2223 samples are measured by using our ARToF-ARPES system while the OPT111 K and OD107.5 K Bi2223 samples are measured by using our laser-ARPES system. To identify bands more clearly, Fig. 2(c) shows the corresponding second-derivative images with respect to the momentum obtained from Fig. 2(b). Two main bands are clearly observed in Figs. 2(b) and 2(c), which are labelled as the OP band (red arrow) and the IP band (blue arrow), corresponding to the OP and IP Fermi surface sheets in Fig. 2(a). The two bands exhibit a systematic evolution with the increasing doping level. First, the separation between the two bands increases with the increase of the doping level. Second, the relative band intensity varies sensitively with the increasing doping level; the OP band gets stronger while the IP band becomes weaker. Third, with increasing doping, the OP band extends to higher binding energy and becomes fully visible in the heavily overdoped samples. Fourth, the OP bands become broad in the heavily overdoped samples (OD108.3 K and OD107.5 K). This is attributed to the enhanced splitting of the OP Fermi surface due to the increased interlayer coupling in the heavily overdoped samples.[16]

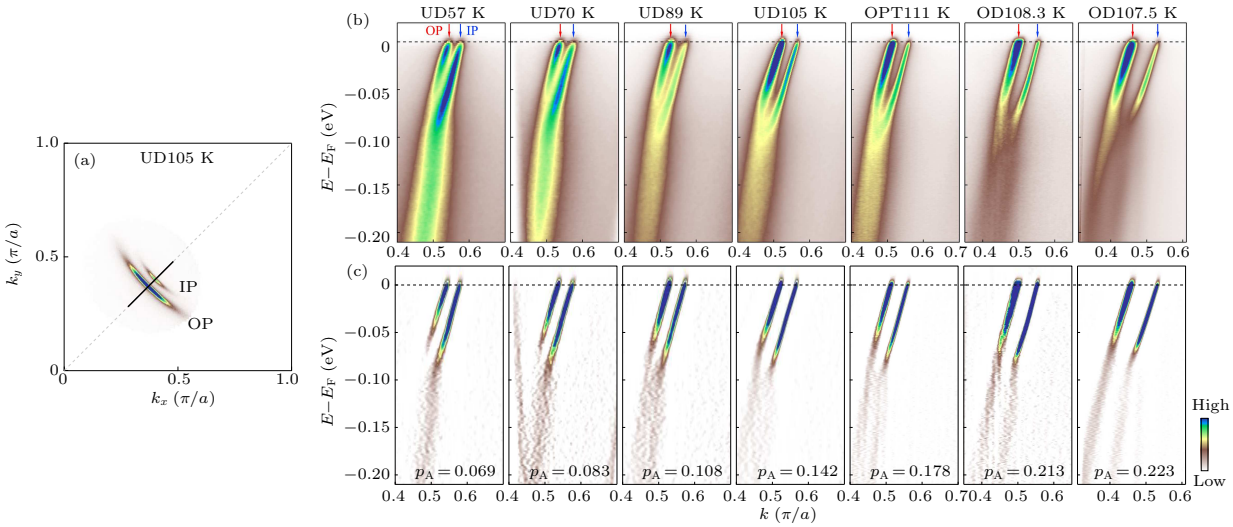


Fig. 2. Band structures measured along the nodal direction at 15 K in Bi2223 samples with different doping levels. (a) Fermi surface mapping measured in the UD105 K Bi2223 sample at 15 K. (b) Band structures measured along the nodal momentum cut in UD57 K, UD70 K, UD89 K, UD105 K, OPT111 K, OD108.3 K and OD107.5 K Bi2223 samples. The location of the nodal momentum cut is indicated by the black line in (a). The OP and IP bands are marked by red and blue arrows, respectively. (c) Corresponding MDC second-derivative images from (b). The doping level (average sample doping p_A) of each sample is indicated in each panel.

To quantitatively determine the band position and the OP–IP band separation, Fig. 3(a) presents momentum distribution curves (MDCs) at the Fermi level in Bi2223 samples with different doping levels obtained from Fig. 2(b). Two main MDC peaks are observed, labelled as OP and IP, which correspond to the OP and IP bands in Fig. 2(b). The positions of these two peaks are presented in Fig. 3(b), together with the results from the previous ARPES measurements.[11,16,17] The momentum separation between the OP and IP bands is plotted in Fig. 3(c). The nodal Fermi momentum k_F for both the OP and IP bands

decreases monotonically with the increasing average doping level (p_A) (Fig. 3(b)). In the meantime, the nodal OP–IP k_F separation increases with the increase of the average doping level (p_A) (Fig. 3(c)). With the establishment of these quantitative relations, it is possible to determine the doping level and T_c of the measured area by measuring its nodal band structure in case the Bi2223 sample is inhomogeneous or doped *in situ* by annealing or surface deposition during ARPES measurements.

Since the doped holes are distributed unevenly among three CuO_2 planes in Bi2223, it is important to know how the charge carriers are quantitatively allocated among the outer and inner CuO_2 planes when the overall doping level changes. Previous ARPES measurements on Bi2223 with different doping levels have provided some information about the charge distribution on the outer and inner CuO_2 planes which are plotted in Fig. 3(d) as empty symbols.[11,16,17] The doping level variation of the outer CuO_2 plane with the average doping level basically follows a linear line crossing the origin (0,0), which can be described as $p_C(\mathrm{OP}) = 1.32p_A$ (red dashed line in Fig. 3(d)). Then the doping level variation of the inner CuO_2 plane can be derived to be $p_C(\mathrm{IP}) = 0.37p_A$ (blue dashed line in Fig. 3(d)). With the establishment of these relations, the charge distribution of our measured samples can be determined as shown by solid circles in Fig. 3(d).

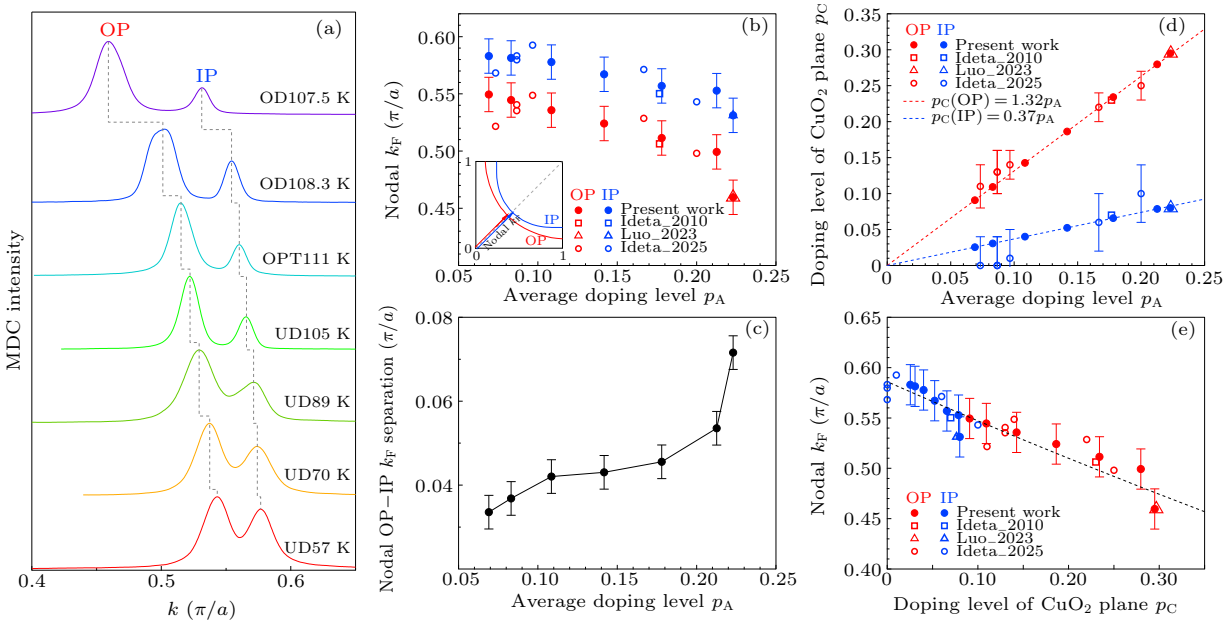


Fig. 3. Doping dependence of the nodal Fermi momentum and the charge distribution in OP and IP CuO_2 planes in Bi2223. (a) MDCs at the Fermi level obtained from Fig. 2(b). (b) The nodal Fermi momentum k_F of the OP (red symbols) and IP (blue symbols) bands obtained from (a) as a function of the average doping level (p_A). The nodal Fermi momentum k_F is defined in the inset of (b). (c) The nodal Fermi momentum difference between the OP and IP bands in our Bi2223 samples. (d) The charge distribution in OP (red symbols) and IP (blue symbols) CuO_2 planes in Bi2223 with different doping levels. The doping levels on the OP CuO_2 planes from the previous ARPES measurements[11,16,17] are fitted by a linear line (red dashed line). Then the doping levels on the IP CuO_2 planes are deduced (blue dashed line). The charge distribution in OP and IP CuO_2 planes in our Bi2223 samples are determined based on the two lines. (e) The nodal Fermi momentum k_F of the OP (red symbols) and IP (blue symbols) bands as a function of the doping level of their corresponding CuO_2 planes (p_C).

After the charge distribution on the OP and IP CuO_2 planes is known from Fig. 3(d), we can replot Fig. 3(b) to show the dependence of the nodal Fermi momentum on the doping level of the individual CuO_2 plane, as shown in Fig. 3(e). The nodal Fermi momentum then follows a similar trend for both the OP and IP CuO_2 planes. It decreases monotonically with the increasing doping level of the CuO_2 plane (p_C). As seen in Fig. 3(d), with increasing average doping level, the doping level difference between the OP and IP CuO_2 planes also increases. According to Fig. 3(e), this will lead to the increase of the nodal OP–IP k_F separation (Fig. 3(c)). Therefore, the increase of the nodal OP–IP k_F separation (Fig. 3(c)) with increasing doping can be attributed to the enhanced charge distribution imbalance between the OP and IP CuO_2 planes in Bi2223.

Now we come to analyze quantitatively the nodal band dispersions in Bi2223. Figures 4(a)–4(g) show dispersions of the OP and IP bands for Bi2223 with different doping levels, obtained by MDC fitting the band structures in Fig. 2(b). Considering the band intensity and the band overlapping, we only present the data that can be reliably extracted from the MDC fitting. Since the IP band in UD57 K and UD70 K samples is dominant (Fig. 2(b)), its dispersion can be obtained up to a high binding energy as shown in Figs. 4(a) and 4(b). For the heavily overdoped OD108.3 K and OD107.5 K samples, the OP and IP bands are well separated and clearly observed (Fig. 2(b)) and their dispersions can also be extracted up to high binding energy, as shown in Figs. 4(f) and 4(g).

The IP band dispersions exhibit a clear kink at ∼ 100 meV in both underdoped (Figs. 4(a) and 4(b)) and heavily overdoped (Figs. 4(f) and 4(g)) Bi2223 samples. The kink effect on the OP band dispersions in the heavily overdoped (Figs. 4(f) and 4(g)) samples is much weaker than that observed in IP band dispersions.

To identify the kink effect and determine the kink position, Figs. 4(h) and 4(i) show the energy difference between the measured IP band dispersion (blue circles in Figs. 4(a) and 4(b)) and the reference line (black dashed lines in Figs. 4(a) and 4(b)) in UD57 K and UD70 K samples. Figures 4(j) and 4(k) show the energy difference between the measured OP (red circles in Figs. 4(f) and 4(g)) and IP (blue circles in Figs. 4(f) and 4(g)) band dispersions and their corresponding reference lines (black dashed lines in Figs. 4(f) and 4(g)) in OD108.3 K and OD107.5 K samples. The energy difference for the IP dispersions (blue circles in Figs. 4(h)–4(k)) shows a peak or hump centered around 94 meV (blue arrows in Figs. 4(h)–4(k)) which is broad in overdoped samples. On the other hand, the energy difference for the OP dispersions (red circles in Figs. 4(j) and 4(k)) is much weaker than that for IP dispersions (blue circles in Figs. 4(j) and 4(k)). They show a weak peak at around 60 meV (red arrows in Figs. 4(j) and 4(k)). The nodal dispersion kink has been commonly observed in single-layer and bilayer cuprates at ∼ 70 meV.[26–30] Further studies show that the 70 meV kink coexists with another 40 meV kink in the nodal dispersions.[31] The kink energy at ∼ 60 meV in the OP nodal band dispersion is comparable to the ∼ 70 meV observed before. However, the kink energy at ∼ 94 meV we observed in the IP dispersion is significantly higher than those (∼ 70 meV and ∼ 40 meV) observed before. The nodal dispersion kinks are generally attributed to electron coupling with bosons and specifically phonons.[26–31] It remains unclear whether the ∼ 70 meV mode corresponds to vibrations of the apical oxygens or in-plane oxygens because their energy scales are similar. Our present study of the dispersion kink in the nodal IP band in Bi2223 may provide new clues to understand the origin of the ∼ 70 meV kink. In single-layer and bilayer cuprates, the Cu in the CuO_2 plane is coordinated with the apical oxygens. But in Bi2223, the Cu in the inner CuO_2 plane is coordinated only with the four in-plane oxygens and no longer coordinated with the apical oxygens (Fig. 1(a)). The unusual kink effect we observed in the IP nodal band dispersion may be related to such a distinct Cu coordination configuration in Bi2223.

Figure 4(l) shows the Fermi velocity of the OP and IP bands in Bi2223 as a function of the doping level of the CuO_2 planes. The Fermi velocity is obtained by fitting the nodal OP and IP band dispersions in Figs. 4(a)–4(g) within the energy range of [−40, 0] meV. The Fermi velocity of both the OP and IP bands shows little variation with the doping level; it is nearly a constant at 1.62 eV·Å. This observation of universal Fermi velocity is consistent with the previous results in single-layer and bilayer cuprates.[30]

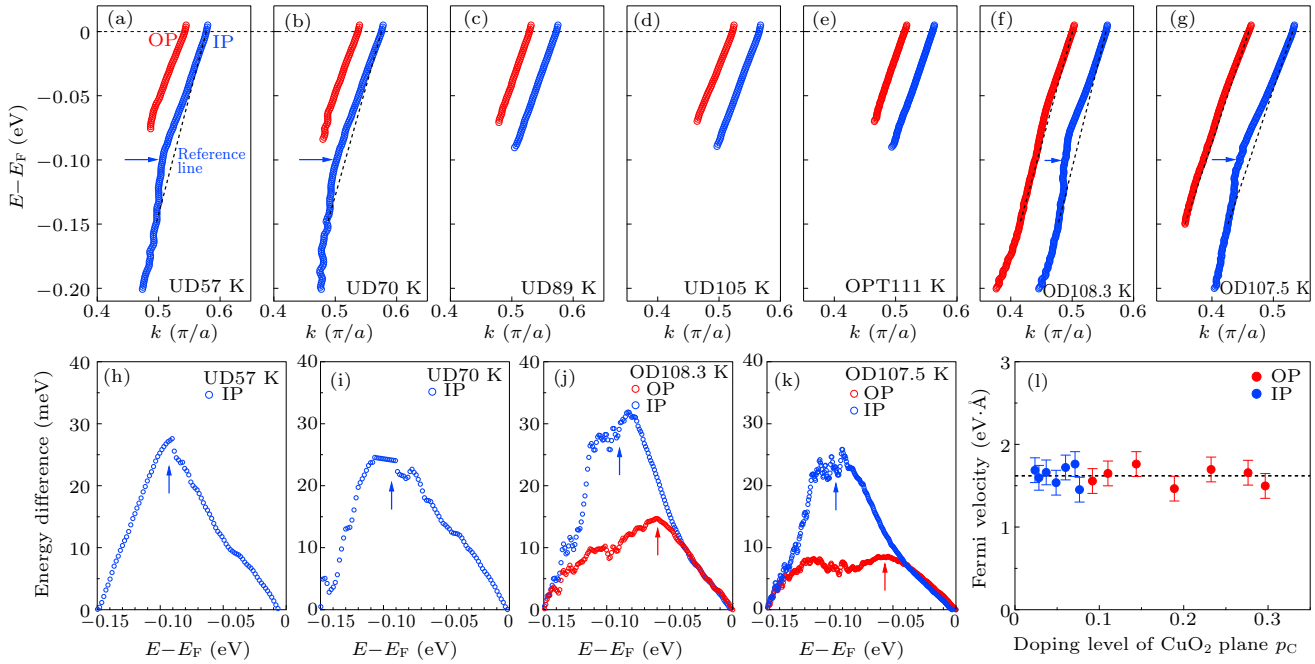


Fig. 4. Nodal electron dynamics in Bi2223 samples with different doping levels. (a)–(g) MDC-derived nodal dispersions for the OP (red cirlces) and IP (blue cirlces) bands in Bi2223 samples with different doping levels. In (a), (b), (f), (g), straight lines are drawn by connecting two points in the related dispersions at the Fermi level and −0.15 eV. (h), (i) The energy difference for the IP bands in UD57 K (h) and UD70 K (i) Bi2223 samples, obtained by subtracting straight lines from the measured IP band dispersions in (a), (b). (j), (k) The energy difference for the OP (red cirlces) and IP (blue cirlces) bands in OD108.3 K and OD107.5 K Bi2223 samples, obtained by subtracting straight lines from the measured OP and IP band dispersions in (f), (g). (l) Doping dependence of the Fermi velocity for the OP and IP bands in Bi2223. The Fermi velocity is obtained by fitting the measured OP and IP band dispersions in (a)–(g) within the energy range of [−40, 0] meV with a linear line. The dashed line shows a constant at 1.62 eV·Å.

In summary, we investigated the doping-dependent nodal electron dynamics in the trilayer cuprate superconductor Bi2223 using high-resolution laser-based ARPES. By preparing samples spanning underdoped to overdoped regions, the electronic phase diagram is established. The nodal Fermi momentum for both outer (OP) and inner (IP) CuO_2 planes decreases monotonically with doping, while their momentum separation increases due to enhanced charge imbalance between the OP and IP planes. The IP band exhibits a prominent ~ 94 meV kink and a weak ~ 60 meV kink is observed in the OP band. The nodal Fermi velocity is nearly constant at ~ 1.62 eV·Å across all doping levels. These results provide important information to understand the origin of high T_c and superconductivity mechanism in high temperature cuprate superconductors.

Acknowledgements

This work is supported by the National Natural Science Foundation of China (Grant Nos. 12488201 by X.J.Z., 12374066 by L.Z., and 12374154 by X.T.L.), the National Key Research and Development Program of China (Grant Nos. 2021YFA1401800 by X.J.Z., 2022YFA1604200 by L.Z., 2022YFA1403900 by G.D.L. and 2023YFA1406000 by X.T.L.), the Strategic Priority Research Program (B) of the Chinese Academy of Sciences (Grant No. XDB25000000 by X.J.Z.), Innovation Program for Quantum Science and Technology (Grant No. 2021ZD0301800 by X.J.Z.), the Youth Innovation Promotion Association of CAS (Grant No. Y2021006 by L.Z.), and the Synergetic Extreme Condition User Facility (SECUF).

References

[1] Chu C W, Deng L Z and Lv B 2015 *Physica C* **514** 290
[2] Scott B A, Suard E Y, Tsuei C C, Mitzi D B, McGuire T R, Chen B H and Walker D 1994 *Physica C* **230** 239
[3] Chakravarty S, Kee H Y and Völker K 2004 *Nature* **428** 53
[4] Iyo A, Tanaka Y, Kito H, Kodama Y, Shirage P M, Shivagan D D, Matsuhata H, Tokiwa K and Watanabe T 2007 *J. Phys. Soc. Jpn.* **76** 094711
[5] Eisaki H, Kaneko N, Feng D L, Damascelli A, Mang P K, Shen K M, Shen Z X and Greven M 2004 *Phys. Rev. B* **69** 064512
[6] Keimer B, Kivelson S A, Norman M R, Uchida S and Zaanen J 2015 *Nature* **518** 179
[7] Fujii T, Terasaki I, Watanabe T and Matsuda A 2002 *Phys. Rev. B* **66** 024507
[8] Piriou A, Fasano Y, Giannini E and Fischer 2008 *Phys. Rev. B* **77** 184508
[9] Feng D L, Damascelli A, Shen K M, Motoyama N, Lu D H, Eisaki H, Shimizu K, Shimoyama J I, Kishio K, Kaneko N, Greven M, Gu G D, Zhou X J, Kim C, Ronning F, Armitage N P and Shen Z X 2002 *Phys. Rev. Lett.* **88** 107001
[10] Ideta S, Takashima K, Hashimoto M, Yoshida T, Fujimori A, Anzai H, Fujita T, Nakashima Y, Ino A, Arita M, Namatame H, Taniguchi M, Ono K, Kubota M, Lu D H, Shen Z X, Kojima K M and Uchida S 2010 *Physica C* **470** S14
[11] Ideta S, Takashima K, Hashimoto M, Yoshida T, Fujimori A, Anzai H, Fujita T, Nakashima Y, Ino A, Arita M, Namatame H, Taniguchi M, Ono K, Kubota M, Lu D H, Shen Z X, Kojima K M and Uchida S 2010 *Phys. Rev. Lett.* **104** 227001
[12] Ideta S, Yoshida T, Fujimori A, Anzai H, Fujita T, Ino A, Arita M, Namatame H, Taniguchi M, Shen Z X, Takashima K, Kojima K and Uchida S 2012 *Phys. Rev. B* **85** 104515
[13] Ideta S, Yoshida T, Hashimoto M, Fujimori A, Anzai H, Ino A, Arita M, Namatame H, Taniguchi M, Takashima K, Kojima K M and Uchida S 2013 *J. Phys.: Conf. Ser.* **428** 012039
[14] Kunisada S, Adachi S, Sakai S, Sasaki N, Nakayama M, Akebi S, Kuroda K, Sasagawa T, Watanabe T, Shin S and Kondo T 2017 *Phys. Rev. Lett.* **119** 217001
[15] Ideta S, Johnston S, Yoshida T, Tanaka K, Mori M, Anzai H, Ino A, Arita M, Namatame H, Taniguchi M, Ishida S, Takashima K, Kojima K M, Devereaux T P, Uchida S and Fujimori A 2021 *Phys. Rev. Lett.* **127** 217004
[16] Luo X Y, Chen H, Li Y H, Gao Q, Yin C H, Yan H T, Miao T M, Luo H L, Shu Y J, Chen Y W, Lin C T, Zhang S J, Wang Z M, Zhang F F, Yang F, Peng Q J, Liu G D, Zhao L, Xu Z Y, Xiang T and Zhou X J 2023 *Nat. Phys.* **19** 1841
[17] Ideta S, Adachi S, Noji T, Yamaguchi S, Sasaki N, Ishida S, Uchida S, Fujii T, Watanabe T, Wang W O, Moritz B, Devereaux T P, Arita M, Mou C Y, Yoshida T, Tanaka K, Lee T K and Fujimori A 2025 arXiv: 2502.16013 [cond-mat.supr-con]
[18] Liu G D, Wang G L, Zhu Y, Zhang H B, Zhang G C, Wang X Y, Zhou Y, Zhang W T, Liu H Y, Zhao L, Meng J Q, Dong X L, Chen C T, Xu Z Y and Zhou X J 2008 *Rev. Sci. Instrum.* **79** 023105
[19] Zhou X J, He S L, Liu G D, Zhao L, Yu L and Zhang W T 2018 *Rep. Prog. Phys.* **81** 062101
[20] Lin C T and Liang B 2002 *New Trends in Superconductivity* (Dordrecht: Springer Netherlands) pp. 19–28
[21] Liang B, Lin C T, Shang P and Yang G 2002 *Physica C* **383** 75
[22] Shimizu K, Okabe T, Horii S, Otzschi K, Shimoyama J and Kishio K 2002 *MRS Online Proc. Libr.* **689** 35
[23] Wei J, Zhang Y, Peng R, Eisaki H and Feng D L 2010 *Physica C* **470** 12
[24] Mukuda H, Shimizu S, Iyo A and Kitaoka Y 2012 *J. Phys. Soc. Jpn.* **81** 011008
[25] Wang Z C, Zou C W, Lin C T, Luo X Y, Yan H T, Yin C H, Xu Y, Zhou X J, Wang Y Y and Zhu J 2023 *Science* **381** 227
[26] Bogdanov P V, Lanzara A, Kellar S A, Zhou X J, Lu E D, Zheng W J, Gu G, Shimoyama J I, Kishio K, Ikeda H, Yoshizaki R, Hussain Z and Shen Z X 2000 *Phys. Rev. Lett.* **85** 2581
[27] Johnson P D, Valla T, Fedorov A V, Yusof Z, Wells B O, Li Q, Moodenbaugh A R, Gu G D, Koshizuka N, Kendziora C, Jian S and Hinks D G 2001 *Phys. Rev. Lett.* **87** 177007
[28] Kaminski A, Randeria M, Campuzano J C, Norman M R, Fretwell H, Mesot J, Sato T, Takahashi T and Kadowaki K 2001 *Phys. Rev. Lett.* **86** 1070
[29] Lanzara A, Bogdanov P V, Zhou X J, Kellar S A, Feng D L, Lu E D, Yoshida T, Eisaki H, Fujimori A, Kishio K, Shimoyama J I, Noda T, Uchida S, Hussain Z and Shen Z X 2001 *Nature* **412** 510
[30] Zhou X J, Yoshida T, Lanzara A, Bogdanov P V, Kellar S A, Shen K M, Yang W L, Ronning F, Sasagawa T, Kakeshita T, Noda T, Eisaki H, Uchida S, Lin C T, Zhou F, Xiong J W, Ti W X, Zhao Z X, Fujimori A, Hussain Z and Shen Z X 2003 *Nature* **423** 398
[31] Yan H T, Bok J M, He J F, Zhang W T, Gao Q, Luo X Y, Cai Y Q, Peng Y Y, Meng J Q, Li C, Chen H, Song C Y, Yin C H, Miao T M, Chen Y W, Gu G D, Lin C T, Zhang F F, Yang F, Zhang S J, Peng Q J, Liu G D, Zhao L, Choi H Y, Xu Z Y and Zhou X J 2023 *Proc. Natl. Acad. Sci. USA* **120** e2219491120